Title

Elastoplastic Dilatant Interface Model for Cyclic Bond-Slip Behavior of Reinforcing Bars

Journal

Journal of Engineering Mechanics, 142(2)

ISSN

0733-9399

Authors

Murcia-Delso, Juan

Shing, P Benson

Publication Date

2016-02-01

DOI

10.1061/(asce)em.1943-7889.0000994

Peer reviewed

Elastoplastic Dilatant Interface Model for Cyclic Bond-Slip Behavior of Reinforcing Bars

Juan Murcia-Delso[1] and P. Benson Shing, M.ASCE[2]

Abstract: This paper presents a new interface model to simulate the cyclic bond-slip behavior of steel reinforcing bars embedded in concrete. A multi-surface plasticity formulation is used to model two major inelastic deformation mechanisms occurring in bond slip. One is the crushing and shearing of the concrete between the bar ribs, and the other is the sliding between the concrete and bar surfaces. These two mechanisms are represented by different yield surfaces and nonassociated flow rules. The flow rules account for the shear dilatation of the interface induced by the wedging action of the bar ribs and crushed concrete particles. The interface model has been implemented in a finite element analysis program and has been validated with experimental data. The model is easy to calibrate and is able to reproduce the bond-slip behavior of bars under a wide range of confinement situations, including bar pullout and concrete splitting failures.
DOI: 10.1061/(ASCE)EM.1943-7889.0000994.

Introduction

The bond-slip behavior of reinforcing bars is an important mechanism to consider when modeling the nonlinear response of reinforced concrete structures, particularly when studying crack opening and spacing in concrete, bar development, and the inelastic deformation capability. Because the chemical adhesion between the concrete and steel can be lost at a relatively low bond stress demand, bond resistance is essentially provided by the bearing forces between the bar ribs and the surrounding concrete and the friction. The American Concrete Institute (ACI 2003) and the International Federation for Structural Concrete (FIB 2000) provide detailed descriptions of these mechanisms and the damage process during bar slip. As the bar slips, the wedging action of the ribs causes a radial expansion of the concrete-steel interface, which activates tensile hoop stresses and causes splitting cracks in the surrounding concrete. When these cracks propagate radially through the concrete cover, the hoop stresses will be lost and the bond resistance drops abruptly. This type of failure is referred to as splitting failure. Splitting failure can be prevented when sufficient concrete cover and/or transverse reinforcement is provided. This will result in a higher bond resistance. In this case, further slip is accommodated by the crushing and shearing of the concrete between the ribs. The accumulation of crushed particles in front of the ribs leads to the expansion of the interface and increases the radial component of the bearing forces, which may result in splitting failure if the concrete cover and the transverse reinforcement are not sufficient to resist the increased demand in hoop stresses. However, when a sufficient confinement is provided and the slip is such that all the concrete between the ribs is completely damaged, only frictional resistance will remain. This type of failure is referred to as pullout failure.

Elastoplastic dilatant interface models can represent the previously mentioned bond-slip mechanisms with high fidelity and reasonable computational cost. This type of model has been extensively used to represent the fracture behavior of quasi-brittle materials (Lotfi and Shing 1994; Carol et al. 1997; Puntel et al. 2006; Caballero et al. 2008; and Koutromanos and Shing 2012). In these formulations, mixed-mode fracture is governed by a failure surface defined in terms of the normal and shear stresses acting on the interface, whereas shear sliding and shear dilatation produced by the wedging action of joint asperities can be modeled with a plastic flow rule. Shear dilatation can also be treated as a geometric phenomenon that can be recovered on slip reversal. However, to accurately represent the wedging mechanism of the bar ribs during bond slip, dedicated dilatant interface formulations are needed because the interface geometry and the damage mechanisms involved are different from those in the fracture process of quasi-brittle materials. Bar slip involves a number of mechanisms including the sliding between the concrete and steel surfaces, the crushing and shearing of the concrete between the ribs, and the opening of transverse cracks at the top of the ribs. To date, only a few such models have been proposed to model the bond-slip behavior. They include the work of Herrmann and Cox (1994), Cox and Herrmann (1998, 1999), Lundgren and Gylltoft (2000), and Serpieri and Alfano (2011).

Herrmann and Cox (1994) and Cox and Herrmann (1998) have proposed an elastoplastic model to represent the bond-slip behavior of reinforcing bars under monotonically increasing loads. Their model features a single yield function that accounts for the variation of the bond stress with the normal stress, and a nonassociated flow rule to simulate shear dilatation. The yield function and flow rule have been calibrated by experimental data. The model has only a few physical parameters to calibrate, and is able to capture the experimentally observed bond-slip behavior of reinforcing bars embedded in concrete with different levels of confinement (Cox and Herrmann 1999). Herrmann and Cox (1994) have also extended their model for cyclic loading by adopting an ad hoc reloading rule to represent the frictional resistance that develops on slip reversal. A similar model has been presented by Lundgren and Gylltoft (2000) for three-dimensional finite element analysis. In this model, a Coulomb yield criterion with a nonassociated flow rule is used to represent the frictional behavior at the interface, and a second yield surface with associated plasticity is used to cap the bond stress

[1]Researcher, Tecnalia Research and Innovation, Parque Cientifico y Tecnologico de Bizkaia, C/ Geldo, Edificio 700, 48160 Derio, Spain (corresponding author). E-mail: juan.murcia@tecnalia.com

[2]Professor, Dept. of Structural Engineering, Univ. of California, San Diego, 9500 Gilman Dr. MC0085, La Jolla, CA 92093-0085.

Note. This manuscript was submitted on August 4, 2014; approved on July 16, 2015; published online on September 2, 2015. Discussion period open until February 2, 2016; separate discussions must be submitted for individual papers. This paper is part of the ***Journal of Engineering Mechanics***, © ASCE, ISSN 0733-9399/04015082(13)/$25.00.

during pullout failure. When the slip does not exceed the previously attained peak during a load reversal, the model has a frictional resistance that is reduced as compared to that for monotonic loading. Their model has been validated by monotonic bond-slip tests and cyclic tests with slip reversals, as well as lap-splice tests and anchorage tests on bars anchored at the ends of a beam (Lundgren and Magnusson 2001). Serpieri and Alfano (2011) have modeled the interaction between a bar and the concrete with three interfaces of different inclinations. The interfaces represent the geometry of the contact surface between the two materials within a representative length unit bounded by two consecutive bar ribs. The behavior of each of these interfaces is modeled by a damage-friction law governing the adhesion and friction. The dilatation and wedging mechanism are governed by the prescribed surface geometry. The model is able to reproduce the bond stress-versus-slip behavior under monotonic and cyclic loading in an approximate manner. However, the concrete crushing and shearing that dominate the pullout failure of a bar are not directly simulated.

A new elastoplastic, dilatant, interface model is proposed in this paper to simulate the cyclic bond-slip behavior of deformed bars under a wide range of confinement situations. The model accounts for two major deformation mechanisms in bond slip, namely, the crushing and shearing of concrete by bar ribs, and the sliding between the concrete and the bar surfaces, as depicted in Fig. 1(a). Plasticity theory is suitable to model these mechanisms because the associated deformations are not recovered on unloading. A multisurface plasticity formulation is adopted with each of the aforementioned mechanisms represented by a separate yield surface and flow rule. The model has been implemented in a finite element program and has been validated by data from monotonic bond-slip tests and cyclic tests with slip reversals under different confinement levels. This paper presents the theoretical formulation, numerical implementation, and experimental validation of the model.

Elastoplastic Interface Formulation

In this formulation, the interaction between a reinforcing bar and the surrounding concrete is simulated with an interface model, as shown in Fig. 1. The relation between the relative displacements, d_n and d_t, in the normal and tangential directions of the interface, and the normal and shear (bond) stresses, σ and τ, at the interface is established with an elastoplastic formulation. The vector of relative displacements, $\mathbf{d} = \{ d_n \quad d_t \}^T$, is decomposed into an elastic part and a plastic part, i.e., $\mathbf{d} = \mathbf{d}^e + \mathbf{d}^p$. The stress vector, $\boldsymbol{\sigma} = \{ \sigma \quad \tau \}^T$, is a linear function of the elastic displacements as follows:

$$\boldsymbol{\sigma} = \mathbf{D}^e \mathbf{d}^e \tag{1}$$

in which $\mathbf{D}^e$ is a diagonal matrix of elastic constants

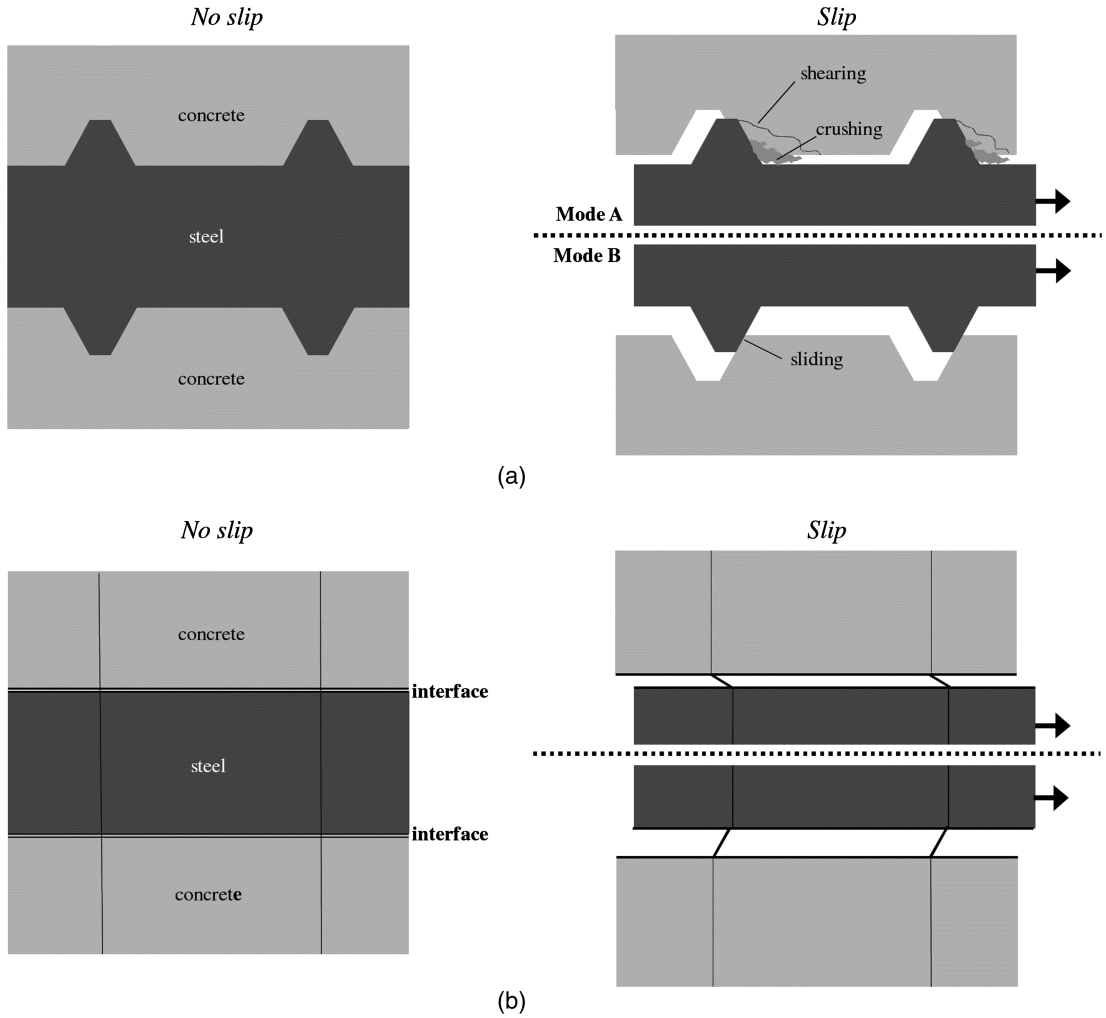

Fig. 1. Bond-slip behavior: (a) bar-concrete interaction; (b) interface model

J. Eng. Mech., 2016, 142(2): 04015082

$$\mathbf{D}^{\mathbf{e}} = \begin{bmatrix} D_{nn} & 0 \\ 0 & D_{tt} \end{bmatrix} \tag{2}$$

The elastic domain is bounded by three yield surfaces that represent the plastic deformation modes associated with bar slip and are described with the following yield criteria:

$$F_A(\boldsymbol{\sigma}, \mathbf{q}) = 0 \qquad F_{B^+}(\boldsymbol{\sigma}, \mathbf{q}) = 0 \qquad F_{B^-}(\boldsymbol{\sigma}, \mathbf{q}) = 0 \tag{3}$$

in which $\mathbf{q} = \{\, p^+ \quad p^- \quad r \quad s \,\}^T$ is a vector of internal variables controlling the evolution of the yield surfaces and the deterioration of bond resistance. The four components of vector $\mathbf{q}$ are described in subsequent sections. Yield function $F_A(\boldsymbol{\sigma}, \mathbf{q})$ is to capture the crushing and shearing of the concrete between bar ribs, which is called Plastic Mode A, as shown in Fig. 1. The other two yield functions, $F_{B^+}(\boldsymbol{\sigma}, \mathbf{q})$ and $F_{B^-}(\boldsymbol{\sigma}, \mathbf{q})$, are used to describe the sliding at the concrete-steel contact surface, which is called Plastic Mode B, also shown in Fig. 1. Mode B is governed by $F_{B^+}(\boldsymbol{\sigma}, \mathbf{q})$ when sliding is in the positive direction (i.e., $\dot{d}_t > 0$) and $F_{B^-}(\boldsymbol{\sigma}, \mathbf{q})$ when sliding is in the negative direction. These yield surfaces are shown in the $\sigma - \tau$ space in Fig. 2(a). Initially, when the slip is zero or very small, the bond resistance is assumed to be provided by friction alone (ignoring the adhesion), governed by failure surfaces $F_{B^+}(\boldsymbol{\sigma}, \mathbf{q})$ and $F_{B^-}(\boldsymbol{\sigma}, \mathbf{q})$. As the bar slips, the wedging action of the bar ribs engages the mechanical interlock between the concrete and the ribs, introducing a radial compressive stress at the interface. If the confinement is not sufficient, radial splitting cracks will develop in the surrounding concrete, the radial compressive stress will disappear, and the bond resistance will be lost. When sufficient confinement is present to prevent the splitting failure of the concrete, the radial compressive stress will increase and the resulting bond resistance will be governed by F_A.

The rate of plastic displacements is defined by a nonassociated flow rule, which can be expressed as follows:

$$\dot{\mathbf{d}}^{\mathbf{p}} = \dot{\lambda}\mathbf{m}(\boldsymbol{\sigma}, \mathbf{q}) \tag{4}$$

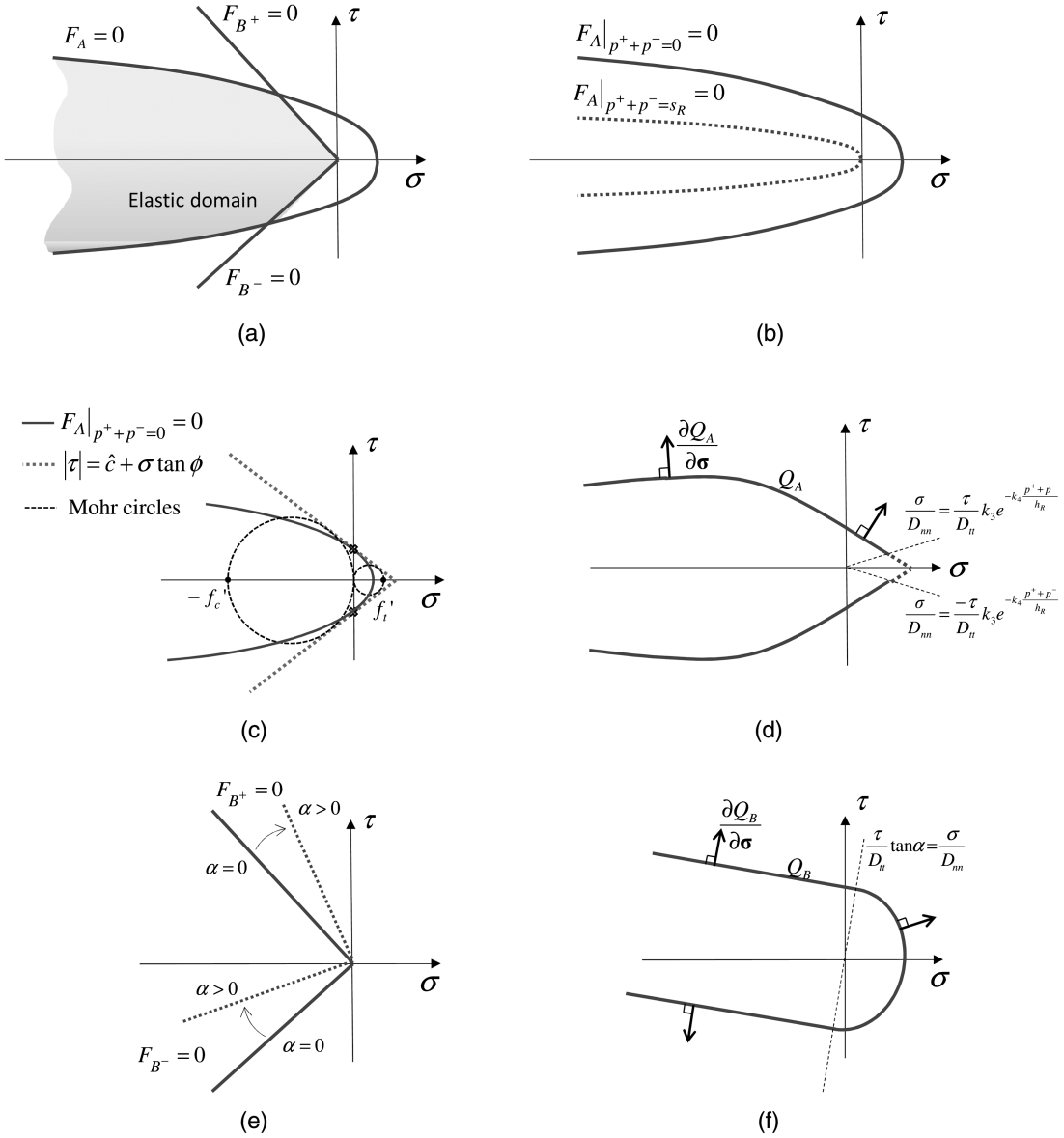

Fig. 2. Yield surfaces and flow rules: (a) yield surfaces and elastic domain; (b) yield surface for Mode A; (c) calibration of yield surface for Mode A; (d) plastic potential for Mode A; (e) yield surface for Mode B; (f) plastic potential for Mode B

J. Eng. Mech., 2016, 142(2): 04015082

where a superposed dot represents rate of change; $\dot{\lambda}$ is a plastic multiplier; and $\mathbf{m}$ is a vector function defining the direction of the plastic flow. The internal variables are functions of the plastic displacements. They are defined in the rate form as follows:

$$\dot{\mathbf{q}} = g(\dot{\mathbf{d}}^p) \tag{5}$$

The yield functions, hardening and softening laws, and flow rules are described with more details in the subsequent sections.

Crushing and Shearing of Concrete between Ribs (Plastic Mode A)

The interlocking action between the concrete and the bar ribs provides most of the bond resistance. However, as the bar slips, this action can lead to the crushing and shearing of the concrete between the ribs, which will reduce the bond resistance and eventually result in the pullout failure of the bar. This slip mechanism is referred to as Plastic Mode A. Based on experimental evidence, such as the data of Malvar (1992), Cox and Herrmann (1998) have concluded that in a pullout failure, the bond resistance increases with the normal confining stress, but that relation is not linear. Hence, to represent the interlocking resistance, the following yield function is proposed

$$F_A = \left|\frac{\tau}{f'_c}\right|^{k_1} - \left(\frac{c}{f'_c}\right)^{k_1} + \mu_A \frac{\sigma}{f'_c} \tag{6}$$

where the stress quantities are normalized by the compressive strength of the concrete, f'_c, in absolute value; c is the shear resistance at $\sigma = 0$; and μ_A and k_1 govern the rate of increase of the shear resistance with respect to the normal stress. The resulting yield surface is shown in Fig. 2(b). The deterioration of the bond resistance resulting from the shearing and crushing of the concrete between the ribs is controlled by the decrease of the values of c and μ_A. The following softening laws are defined to control the evolution of c and μ_A, which causes the yield surface to shift and shrink in the stress space, as shown in Fig. 2(b)

$$c = c_0 \left\langle 1 - \frac{p^+ + p^-}{s_R} \right\rangle \tag{7a}$$

$$\mu_A = \mu_{A,0} e^{-k_2[(p^+ + p^-)/s_R]} \tag{7b}$$

where $\langle\cdot\rangle$ are Macaulay brackets; c_0 is the initial value of c; $\mu_{A,0}$ is the initial value of μ_A; s_R is the clear rib spacing; k_2 is a constant controlling the rate of decrease of the value of μ_A; and p^+ and p^- are internal variables representing the absolute values of the cumulative plastic tangential displacements (slips) associated with Mode A in the positive and negative directions, respectively. The values of p^+ and p^- are computed from the increments of plastic tangential displacement, $\dot{d}_t^p|_A$, associated with Mode A, as follows:

$$\dot{p}^+ = \langle \dot{d}_t^p|_A \rangle \tag{8a}$$

$$\dot{p}^- = \langle -\dot{d}_t^p|_A \rangle \tag{8b}$$

In Eq. (8), $\dot{d}_t^p|_A = \dot{d}_t^p$ when Mode A is active, and $\dot{d}_t^p|_A = 0$ otherwise. The rate of the normal plastic displacement $\dot{d}_n^p|_A$ is defined in the same way. As shown in Eq. (7a), c is assumed to decay linearly to zero as the total bar slip, $p^+ + p^-$, caused by Mode A approaches the clear rib spacing, s_R, at which all the concrete between the ribs is totally damaged by crushing and shearing. At this stage, only the frictional resistance remains. As shown in Eq. (7b), μ_A diminishes to zero exponentially as the total bar slip in Mode A increases, representing the smoothening of the interface.

Parameters c_0 and $\mu_{A,0}$ in the yield function are calibrated by assuming that under a low confinement stress, the crushing and shearing failure of concrete is governed by the Mohr-Coulomb law with a cohesion parameter, $\hat{c}$, and an internal friction angle, ϕ, as shown in Fig. 2(c). These two parameters can be expressed in terms of the concrete compressive strength, f'_c, and tensile strength, f'_t, as follows:

$$\hat{c} = 0.5\sqrt{f'_c f'_t} \tag{9a}$$

$$\phi = \sin^{-1}\left(\frac{f'_c - f'_t}{f'_c + f'_t}\right) \tag{9b}$$

With this assumption, the initial yield surface for Mode A is set to be tangent to the Mohr-Coulomb failure surface at $\sigma = 0$, as shown in Fig. 2(c). As a result, c_0 and $\mu_{A,0}$ are determined as

$$c_0 = 0.5\sqrt{f'_c f'_t} \tag{10a}$$

$$\mu_{A,0} = 0.5^{k_1} k_1 (f'_c - f'_t) f_c'^{-0.5k_1} f_t'^{(0.5k_1 - 1)} \tag{10b}$$

Malvar (1992) has observed in his tests that bar slip will initially induce a radial expansion of the surrounding concrete, which is then followed by a small contraction as the bar slips. This behavior can be explained by the dislocation of crushed concrete particles at the interface and the smoothening of the particles caused by the grinding action. To account for this phenomenon, the following plastic flow vector, defined as the gradient of a plastic potential Q_A, is proposed for Mode A:

$$\mathbf{m}_A = \begin{Bmatrix} m_{A,1} \\ m_{A,2} \end{Bmatrix} = \begin{Bmatrix} k_3 \left\langle 1 - \frac{\langle -\sigma \rangle}{f'_c} \right\rangle e^{-k_4 \frac{p^+ + p^-}{h_R}} - k_5 \frac{\langle -\sigma \rangle}{f'_c} \frac{\langle r \rangle}{h_R} \\ 1 \cdot \text{sign}(\tau) \end{Bmatrix} \tag{11}$$

where k_3, k_4, and k_5 are constants; h_R is the height of the ribs; and r is an internal variable that represents the net interface opening caused by the shearing and crushing of concrete between the ribs. Initially, r is zero, and its evolution depends on the increment of the plastic normal displacement, $\dot{d}_n^p|_A$, associated with Mode A as follows:

$$\dot{r} = \dot{d}_n^p|_A \tag{12}$$

The first term in the expression for $m_{A,1}$ in Eq. (11) represents the dilatation, i.e., the normal displacement caused by the dislocation of the crushed concrete particles. This dilatation effect diminishes linearly as the magnitude of the normal confining stress (normalized by the compressive strength of concrete) increases and decreases exponentially as the total bar slip (normalized by the rib height) associated with this plastic mode increases. The second term in the expression for $m_{A,1}$ accounts for the loss of crushed concrete particles (compaction) as the concrete is severely damaged. Compaction is more significant when the magnitude of the normalized confining stress and the net opening of the interface normalized by the rib height increase. As Eq. (11) implies, the rate of compaction will become zero when r is zero. Hence, net interface compaction will not occur. These phenomena are consistent with the experimental observations of Malvar (1992).

The plastic potential Q_A is shown in Fig. 2(d). The direction of the plastic flow given by Eq. (11) is discontinuous and undefined at $\tau = 0$. The flow rule would have to be modified to allow a correct stress return to the tip of the yield surface at $(\sigma_{\text{tip}}, 0)$. However, that

condition should never occur because the stress return to the tip of the yield surface for Mode A will violate the yield condition for Mode B when $\sigma_{\text{tip}} > 0$, as shown in Fig. 2(a). To avoid this situation, when $\sigma^e/D_{nn} \geq (|\tau^e|/D_{tt}) \cdot k_3 e^{-k_4(p^+ + p^-)/h_R}$, the model will be switched from Mode A to Mode B. In that situation, the plastic flow direction for Mode B will be given by Eq. (17*c*) for reasons to be explained in the following section. The previously described condition will ensure a smooth transition of the flow direction.

Sliding at the Concrete-Steel Surface (Plastic Mode B)

At a low normal confining stress, it is assumed that bar slip is caused by the sliding of the bar with respect to the concrete, and the sliding resistance is governed by the Coulomb law with a constant coefficient of friction μ_B. The contact between the concrete and steel can take place on the inclined surface of the ribs, or on a plane parallel to the bar axis, either on the barrel of the bar between the ribs or on top of the ribs. The Coulomb law for sliding along a planar surface is

$$|\tau'| = \mu_B \sigma' \tag{13}$$

where σ' and τ' are the normal and shear stresses on the sliding surface. When the sliding surface has an angle of inclination, α, with respect to the axis of the bar, the Coulomb law can be expressed in terms of the normal and shear stresses, σ and τ, perpendicular and parallel to the axis of the bar as follows:

$$|\tau \cos\alpha + \sigma \sin\alpha| + \mu_B(\sigma \cos\alpha - \tau \sin\alpha) = 0 \tag{14}$$

where angle α is positive for the surface on the left side of a rib and negative for the surface on the right. A rearrangement of Eq. (14) leads to two yield conditions. For the sliding of the concrete toward right, which is defined as positive sliding, one has the following yield condition:

$$F_{B^+} = \tau + \mu_{B^+\text{eff}}\sigma = 0 \tag{15a}$$

where $\mu_{B^+\text{eff}}$ is the effective friction coefficient for positive sliding, which depends on the coefficient of friction μ_B of the contact surface and angle α. For $\cos\alpha > 0$ and $\tan\alpha < 1/\mu_B$, $\mu_{B^+\text{eff}}$ is equal to

$$\mu_{B^+\text{eff}} = \frac{\mu_B \cos\alpha + \sin\alpha}{\cos\alpha - \mu_B \sin\alpha} \tag{15b}$$

For negative sliding (i.e., concrete sliding toward the left), the yield condition can be expressed as

$$F_{B^-} = -\tau + \mu_{B^-\text{eff}}\sigma = 0 \tag{16a}$$

where $\mu_{B^-\text{eff}}$ is the effective friction coefficient for negative sliding. For $\cos\alpha > 0$ and $\tan\alpha > -1/\mu_B$, $\mu_{B^-\text{eff}}$ is equal to

$$\mu_{B^-\text{eff}} = \frac{\mu_B \cos\alpha - \sin\alpha}{\cos\alpha + \mu_B \sin\alpha} \tag{16b}$$

The yield surfaces for sliding are two straight lines as shown in Fig. 2(e). These lines rotate about the origin of the $\sigma - \tau$ space as α changes.

The plastic displacements in Mode B are associated with the sliding on the contact plane whose slope is defined by angle α, which can be zero, a positive value, or a negative value depending on the position of contact between the concrete and the bar surface. Accordingly, the direction of the plastic flow vector for Mode B is given by the following expressions. For F_{B^+}

$$\mathbf{m}_{B^+} = \begin{Bmatrix} m_{B,1} \\ m_{B,2} \end{Bmatrix} = \begin{Bmatrix} \tan\alpha \\ 1 \end{Bmatrix} \tag{17a}$$

and for F_{B^-}

$$\mathbf{m}_{B^-} = \begin{Bmatrix} m_{B,1} \\ m_{B,2} \end{Bmatrix} = -\begin{Bmatrix} \tan\alpha \\ 1 \end{Bmatrix} \tag{17b}$$

However, when the elastic trial stresses, $\boldsymbol{\sigma}^e$, computed in the stress update are such that $(\tau^e/D_{tt})\tan\alpha < (\sigma^e/D_{nn})$, the plastic flow vector is modified as follows to ensure a smooth transition between the plastic flow directions defined in Eqs. (17*a*) and (17*b*):

$$\mathbf{m}_B = \begin{Bmatrix} m_{B,1} \\ m_{B,2} \end{Bmatrix} = \begin{Bmatrix} \dfrac{\sigma^e}{D_{nn}} \\ \dfrac{\tau^e}{D_{tt}} \end{Bmatrix} \tag{17c}$$

With Eq. (17*c*), stresses are returned to the intersection point of the yield surfaces F_{B^+} and F_{B^-} at the origin of the stress space. The plastic potential Q_B and the direction of the plastic flow, $\partial Q_B/\partial\boldsymbol{\sigma}$, for Mode B defined by Eqs. (17*a*)–(17*c*) are shown in Fig. 2(f). This plastic potential is analogous to that proposed by Puntel et al. (2006) for joint and crack interfaces in quasi-brittle materials.

The value of α is a function of the level of sliding and this function is determined by the initial shape of the sliding surface as shown in Fig. 3, which is governed by the geometry of the surface deformation of the bar, and the damage inflicted on the concrete between the ribs. The value of α is positive when the contact is on the right inclined surface and negative on the left inclined surface shown in Fig. 3. When sliding toward the positive direction on the right surface, the normal displacement will increase. The normal displacement will also increase when sliding toward the negative direction on the left surface. These are represented by Eq. (17). The angle α is assumed to be a function of the maximum inclination angle, α_o, and the horizontal distance, l_I, of an inclined plane, as illustrated in Fig. 3. Distances l_T, as shown in the figure, represent transition zones in which the inclination angle is assumed to vary linearly with the horizontal distance. With the assumption that $l_T = 0.05 l_I$, l_I is related to h_R and α_0 by the expression $l_I = h_R/(0.9\tan\alpha_0 - 0.05\ln|\cos\alpha_0|/\alpha_0)$. When Plastic Mode A is activated, the shape of the sliding surface for Mode B is modified to reflect damage induced on the concrete between the ribs. The crushing and shearing of the concrete is modeled by the increase

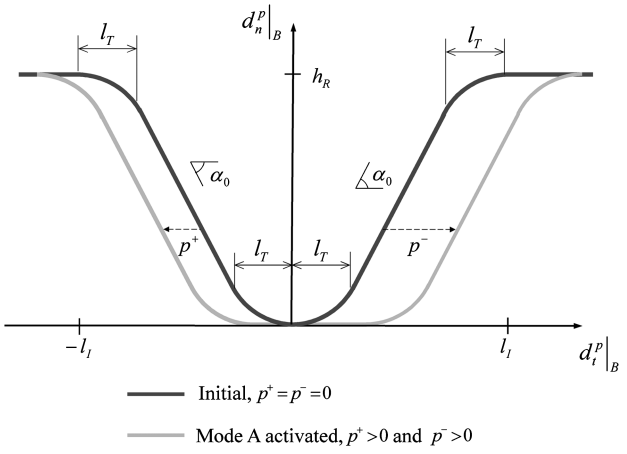

Fig. 3. Sliding surface

J. Eng. Mech., 2016, 142(2): 04015082

of horizontal gaps between the concrete and the ribs, as shown in Fig. 3. The total gap distance is equal to the maximum bar slip caused by Mode A, i.e., p^+ and p^-. With the aforementioned considerations and assumptions, the angle of inclination, α, is represented by the following equation:

$$\alpha(s) = \begin{cases} 0 & s + p^+ \le -l_I \\ \alpha_0 \frac{s - l_I + p^+}{l_T} & -l_I < s + p^+ \le -l_I + l_T \\ -\alpha_0 & -l_I + l_T < s + p^+ \le -l_T \\ \alpha_0 \frac{s + p^+}{l_T} & -l_T < s + p^+ \le 0 \\ 0 & -p^+ < s \le p^- \\ \alpha_0 \frac{s - p^-}{l_T} & 0 < s - p^- \le l_T \\ \alpha_0 & l_T < s - p^- \le l_I - l_T \\ \alpha_0 \frac{l_I - s + p^-}{l_T} & l_I - l_T < s - p^- \le l_I \\ 0 & s - p^- > l_I \end{cases} \tag{18}$$

where s is an internal variable that represents the bar slip caused by Plastic Mode B. The value of s is initially zero, and its rate of change is equal to that of the plastic tangential displacement, $\dot{d}_t^p|_B$, associated with Mode B, as follows:

$$\dot{s} = \dot{d}_t^p|_B \tag{19}$$

where $\dot{d}_t^p|_B = \dot{d}_t^p$ when Mode B is active, and $\dot{d}_t^p|_B = 0$ otherwise.

Numerical Implementation

A stress update algorithm has been developed to solve the constitutive relations numerically as explained subsequently. Given the stress vector $\boldsymbol{\sigma}_m$, internal variables $\mathbf{q}_m$, displacement $\mathbf{d}_m$, and displacement increment $\Delta\mathbf{d}$ at step m, it is necessary to determine the stresses $\boldsymbol{\sigma}_{m+1}$ and internal variables $\mathbf{q}_{m+1}$ at step $m+1$. For this purpose, an elastic predictor-plastic corrector algorithm is used. The stress update is a two-step procedure as shown in Eqs. (20) and (21). First, the elastic predictor stresses are calculated

$$\boldsymbol{\sigma}_{m+1}^e = \boldsymbol{\sigma}_m + \mathbf{D}^{\mathbf{e}} \Delta\mathbf{d} \tag{20}$$

If the elastic prediction in Eq. (20) satisfies $F_i(\boldsymbol{\sigma}_m^e, \mathbf{q}_m) \le 0$, it is an admissible solution and

$$\boldsymbol{\sigma}_{m+1} = \boldsymbol{\sigma}_{m+1}^e \tag{21a}$$

Otherwise, a plastic correction needs to be applied as follows:

$$\boldsymbol{\sigma}_{m+1} = \boldsymbol{\sigma}_{m+1}^e - \mathbf{D}^{\mathbf{e}} \Delta\mathbf{d}^p \tag{21b}$$

The increment of the plastic displacements, $\Delta\mathbf{d}^p$, in Eq. (21*b*) is obtained with the generalized trapezoidal rule (Ortiz and Popov 1985), which results in the following equation:

$$\boldsymbol{\sigma}_{m+1} = \boldsymbol{\sigma}_{m+1}^e - \Delta\lambda \mathbf{D}^{\mathbf{e}} [(1-\theta)\mathbf{m}_m + \theta \mathbf{m}_{m+1}] \tag{22}$$

where $0 \le \theta \le 1$. The internal variables are also updated in the same fashion.

$$\mathbf{q}_{m+1} = \mathbf{q}_m + g\{\Delta\lambda[(1-\theta)\mathbf{m}_m + \theta \mathbf{m}_{m+1}]\} \tag{23}$$

The elastic predictor-plastic corrector method presents a set of nonlinear equations, which has to be solved iteratively to find $\Delta\lambda$ that will satisfy the condition that $F_i(\boldsymbol{\sigma}_{m+1}, \mathbf{q}_{m+1}) = 0$, as well as Eqs. (22) and (23). The exact forms of Eqs. (22) and (23) depend on the yield surface and flow rule used for the plastic correction. The plastic correction is to bring the stress state from the elastic prediction back to the yield surface. Fig. 4 shows three possible stress return scenarios for $\tau > 0$: (1) return to the yield surface corresponding to Mode A ($F_A = 0$); (2) return to the yield surface corresponding to Mode B ($F_{B^+} = 0$); and (3) return to the intersection of the previously noted two yield surfaces ($F_A = F_{B^+} = 0$). Similar return possibilities exist for $\tau < 0$.

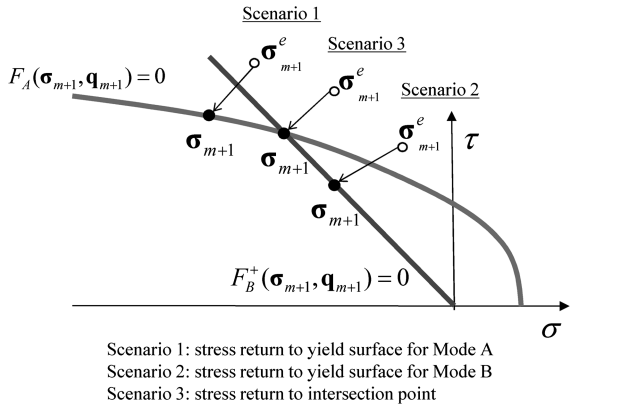

Fig. 4. Possible stress-return scenarios for plastic correction

Fig. 5 shows the flowchart of the stress update algorithm. The algorithm adopts an objective stress return strategy so that the solution will not depend on which yield condition is checked first. In this strategy, when the elastic trial stresses lie outside both yield surfaces, two possible stress return scenarios are individually considered as the first step: stress return to the surface for Mode A, and stress return to the surface for Mode B. The stress return that satisfies both conditions that $F_A \le 0$ and $F_{B^+} \le 0$ (or $F_{B^-} \le 0$) will be the admissible solution. If neither of the two stress returns satisfies both conditions, or if both stress returns satisfy the two conditions, then the stresses are returned to the intersection of these two yield surfaces. However, in Mode A, if the elastic trial stresses are such that

$$\sigma_{m+1}^e / D_{nn} \ge (|\tau_{m+1}^e| / D_{tt}) k_3 e^{-k_4(p^+ + p^-)/h_R} \tag{24}$$

Mode B will be activated. When the elastic predictor stress state is outside one of the yield surfaces only, stress correction is made for that yield surface. If this stress return violates the other yield surface, then it is invalid and the stresses are returned to the intersection point of the two yield surfaces. The solution procedures corresponding to each of the three possible stress return scenarios are presented in the subsequent sections.

Stress Return to Yield Surface corresponding to Mode A

To have the stress state returned to the yield surface corresponding to Mode A, the plastic correction based on the trapezoidal rule is

$$\sigma_{m+1} = \sigma_{m+1}^e - \Delta\lambda D_{nn}[(1-\theta) m_{A,1}(\sigma_m, \tau_m, \mathbf{q}_m) + \theta m_{A,1}(\sigma_{m+1}, \tau_{m+1}, \mathbf{q}_{m+1})] \tag{25a}$$

$$\tau_{m+1} = \tau_{m+1}^e - \Delta\lambda D_{tt} \text{sign}(\tau) \tag{25b}$$

The internal variables associated with Mode A are updated as follows:

J. Eng. Mech., 2016, 142(2): 04015082

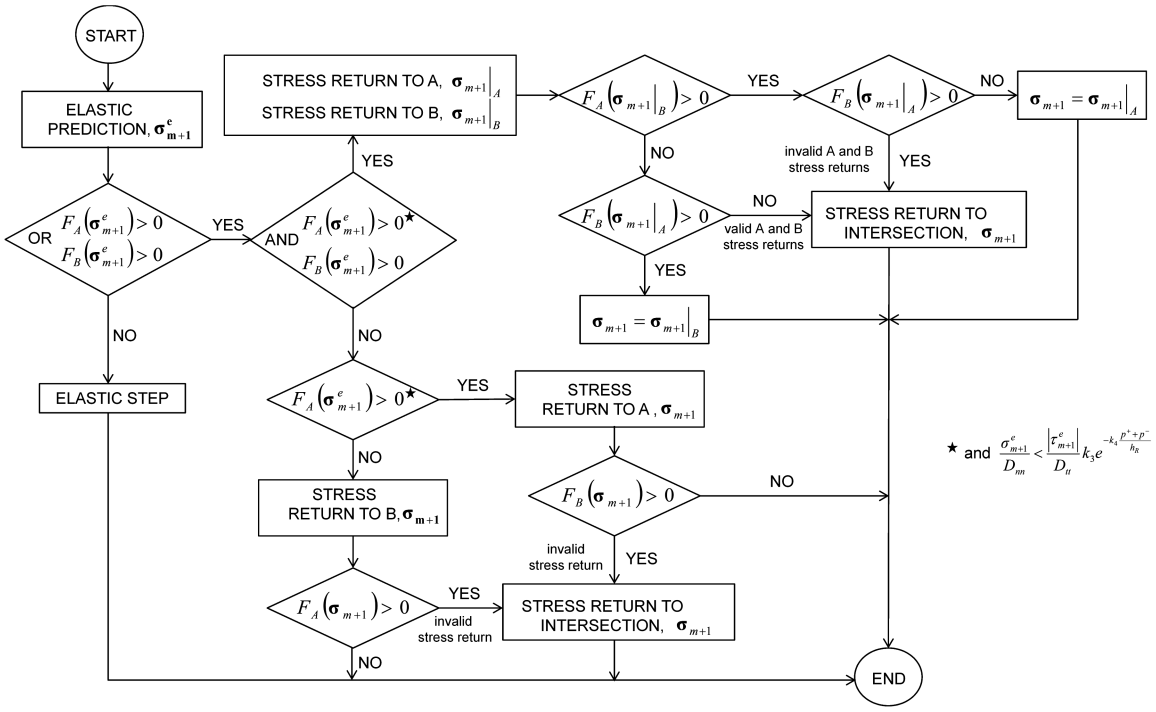

Fig. 5. Flowchart of the stress return algorithm

$$p^{+}_{m+1} = p^{+}_{m} + \Delta\lambda\langle 1 \cdot \mathrm{sign}(\tau)\rangle \tag{26a}$$

$$p^{-}_{m+1} = p^{-}_{m} + \Delta\lambda\langle -1 \cdot \mathrm{sign}(\tau)\rangle \tag{26b}$$

$$r_{m+1} = r_m + \Delta\lambda[(1-\theta)m_{A,1}(\sigma_m, \tau_m, \mathbf{q}_m) + \theta m_{A,1}(\sigma_{m+1}, \tau_{m+1}, \mathbf{q}_{m+1})] \tag{26c}$$

The value of $\Delta\lambda$ is to be evaluated iteratively until the condition that $F_A(\boldsymbol{\sigma}_{m+1}, \mathbf{q}_{m+1}) = 0$ and Eqs. (25) and (26) are satisfied. For this purpose, an iterative bracketing strategy has been followed. The solution for $\Delta\lambda$ is bracketed with a lower bound value and an upper bound value that result in $F_A > 0$ and $F_A < 0$, respectively. This bracket is updated with the bisection method until the result converges to $F_A(\boldsymbol{\sigma}_{m+1}, \mathbf{q}_{m+1}) = 0$.

In the iterative bracketing scheme, the values of $\boldsymbol{\sigma}_{m+1}$ and $\mathbf{q}_{m+1}$ are updated with Eqs. (25) and (26). Because Eqs. (25*a*) and (26*c*) are nonlinear and implicit with respect to σ_{m+1} and r_{m+1}, they need to be solved iteratively to obtain values of σ_{m+1} and r_{m+1} for a given value of $\Delta\lambda$, with the initial values of σ_{m+1} and r_{m+1} being σ_m and r_m, respectively.

Stress Return to Yield Surface corresponding to Mode B

For Mode B, the plastic correction of the stress state is given by

$$\sigma_{m+1} = \sigma^{e}_{m+1} - \Delta\lambda D_{nn}[(1-\theta)m_{B,1}(\mathbf{q}_m) + \theta m_{B,1}(\mathbf{q}_{m+1})] \tag{27a}$$

$$\tau_{m+1} = \tau^{e}_{m+1} - \Delta\lambda D_{tt} \text{ (if the stresses are returned to } F_{B^+} = 0) \tag{27b}$$

$$\tau_{m+1} = \tau^{e}_{m+1} + \Delta\lambda D_{tt} \text{ (if the stresses are returned to } F_{B^-} = 0) \tag{27c}$$

and the internal variable that needs to be updated is the slip caused by Mode B.

$$s_{m+1} = s_m + \Delta\lambda \text{ (if the stresses are returned to } F_{B^+} = 0) \tag{28a}$$

$$s_{m+1} = s_m - \Delta\lambda \text{ (if the stresses are returned to } F_{B^-} = 0) \tag{28b}$$

The nonlinear solution for $\Delta\lambda$ to satisfy $F_B(\boldsymbol{\sigma}_{m+1}, \mathbf{q}_{m+1}) = 0$ and Eqs. (27) and (28) is obtained with the bisection bracketing method as previously described. However, if $\frac{\tau^{e}_{m+1}}{D_{tt}} \tan\alpha_m < \frac{\sigma^{e}_{m+1}}{D_{nn}}$, the stresses are directly returned to the origin of the stress space according to the plastic flow vector defined in Eq. (17*c*), i.e.,

$$\sigma_{m+1} = \tau_{m+1} = 0 \tag{29}$$

Accordingly, the increment of the plastic displacement has to be $\Delta\mathbf{d}^p = \{\, \sigma^{e}_{m+1}/D_{nn} \quad \tau^{e}_{m+1}/D_{tt} \,\}^T$, and the slip caused by Mode B is

$$s_{m+1} = s_m + \frac{\tau^{e}_{m+1}}{D_{tt}} \tag{30}$$

Stress Return to Intersection of Two Yield Surfaces

The stress return to the intersection of the yield surfaces corresponding to Modes A and B requires a special treatment. For this case, the plastic correction is considered as a linear combination of the corrections obtained with the flow rules for Mode A and Mode B, respectively. Hence, the plastic correction of the stress state is given by

$$\sigma_{m+1} = \sigma^e_{m+1} - \Delta\lambda_1 D_{nn}[(1-\theta)m_{A,1}(\sigma_m, \tau_m, \mathbf{q}_m) + \theta m_{A,1}(\sigma_{m+1}, \tau_{m+1}, \mathbf{q}_{m+1})] - \Delta\lambda_2 D_{nn}[(1-\theta)m_{B,1}(\mathbf{q}_m) + \theta m_{B,1}(\mathbf{q}_{m+1})] \quad (31a)$$

$$\tau_{m+1} = \tau^e_{m+1} - \Delta\lambda_1 D_{tt} - \Delta\lambda_2 D_{tt} \quad \text{(if the stresses are returned to } F_{B^+} = 0) \quad (31b)$$

$$\tau_{m+1} = \tau^e_{m+1} - \Delta\lambda_1 D_{tt} + \Delta\lambda_2 D_{tt} \quad \text{(if the stresses are returned to } F_{B^-} = 0) \quad (31c)$$

The internal variables are calculated as

$$p^+_{m+1} = p^+_m + \langle \Delta\lambda_1 \text{sign}(\tau) \rangle \quad (32a)$$

$$p^-_{m+1} = p^-_m + \langle -\Delta\lambda_1 \text{sign}(\tau) \rangle \quad (32b)$$

$$r_{m+1} = r_m + \Delta\lambda_1[(1-\theta)m_{A,1}(\sigma_m, \tau_m, \mathbf{q}_m) + \theta m_{A,1}(\sigma_{m+1}, \tau_{m+1}, \mathbf{q}_{m+1})] \quad (32c)$$

$$s_{m+1} = s_m + \Delta\lambda_2 \quad \text{(if the stresses are returned to } F_{B^+} = 0) \quad (32d)$$

$$s_{m+1} = s_m - \Delta\lambda_2 \quad \text{(if the stresses are returned to } F_{B^-} = 0) \quad (32e)$$

Eqs. (31*a*) and (32*c*) are nonlinear and implicit with respect to σ_{m+1} and r_{m+1}. Hence, for a given value of $\Delta\lambda_1$, they need to be solved iteratively like Eqs. (25*a*) and (26*c*).

An algorithm has been developed to solve the nonlinear problem to satisfy both yield conditions, $F_A(\boldsymbol{\sigma}_{m+1}, \mathbf{q}_{m+1}) = 0$ and $F_{B^+/B^-}(\boldsymbol{\sigma}_{m+1}, \mathbf{q}_{m+1}) = 0$, and Eqs. (31) and (32). The algorithm consists of two nested loops that employ the bisection bracketing method to solve a system of two equations for two unknowns, $\Delta\lambda_1$ and $\Delta\lambda 2$. In the internal loop, $\Delta\lambda_1$ is kept constant, and the value of $\Delta\lambda 2$ that satisfies $F_{B^+/B^-}(\boldsymbol{\sigma}_{m+1}, \mathbf{q}_{m+1}) = 0$ is determined with the bracketing method. In the external loop, with the value of $\Delta\lambda 2$ determined in the internal loop, the bracketing method is applied to $\Delta\lambda_1$ to satisfy $F_A(\boldsymbol{\sigma}_{m+1}, \mathbf{q}_{m+1}) = 0$. The process is repeated until convergence is reached.

Model Calibration

The model proposed in this paper includes parameters that depend on the diameter and the geometry of the surface deformation of the bar (d_b, h_R, and s_R) and the mechanical properties of the concrete (f'_c and f'_t). The rest are dimensionless parameters that have been calibrated with experimental results of Malvar (1992). These experiments provide data to quantify the relations between the stresses and relative displacements at the concrete-steel interface. They consist of bond-slip tests on 19-mm-diameter bars embedded in presplit concrete cylinders subjected to a constant radial stress. During the tests, the average bond stress, the slip, and the radial displacement were measured. Two series of five tests each were conducted for two types of bars with slightly different rib patterns. For each test series, five different levels of confinement were used, ranging from 3.45 MPa to 31.03 MPa. In all the cases, the bond failed by the pullout of the bars, and crushed concrete was observed between the ribs.

Table 1. Bar and Concrete Properties

Test specimen	d_b (mm)	h_R (mm)	s_R (mm)	f'_c (MPa)	f'_t (MPa)
Malvar (1992), Tests 1, 3, 5	19	0.78	9.2	40.2	4.9
Malvar (1992), Tests 6, 8, 10	19	0.84	10.2	38.4	4.7
Lundgren (2000)	16	0.8[a]	8.0[b]	36	3.6[c]
Murcia-Delso et al. (2013)	43	2.3	24.9	34.5/55.0	2.9/3.8
Metelli and Plizzari (2014), 16-mm bar	16	0.7	9.0	42.7	3.4
Metelli and Plizzari (2014), 20-mm bar	20	0.9	11.4	42.7	3.4

[a]Information not available, estimated as 5% of the bar diameter.
[b]Information not available, estimated as 50% of the bar diameter.
[c]Information not available, estimated as 10% of the compressive strength of concrete.

Table 2. Model Parameters with Fixed Values

Parameter	Value
k_1	2.5
k_2	2.2
k_3	1.0
k_4	2.5
k_5	0.05
μ_B	0.2
α_0	62°

The experimental results have been replicated with the interface model presented in this paper. The values of the model parameters related to the bar geometry and concrete strength have been determined from the information reported in Malvar (1992) and are presented in Table 1. The dimensionless parameters have been so calibrated to match the experimental results. Their values are presented in Table 2. The values of k_i in Table 2 are independent of the bar and concrete properties as they are coefficients associated with the normalized bar and concrete properties. The value of μ_B obtained from this calibration (0.2) is smaller than values typically assumed for the friction coefficient between steel and concrete, which range between 0.4 and 0.5.

The values of μ_B and α_0 in Table 2 satisfy the conditions for which Eqs. (15*b*) and (16*b*) are valid. Their values may depend on the surface conditions of the bar, but the range of their possible variations is expected to be small and the subsequent validation study shows that they can be assumed to be constants. The values in Table 2 are based on data obtained from reinforcing bars with normal rib geometry. Bars with a high relative rib area may have different values for these parameters. The elastic constants for the interface model also need to be calibrated. The elastic tangential stiffness is taken as $D_{tt} = 0.04E_c/d_b$, in which E_c is the Young's modulus of the concrete and d_b is the bar diameter, as suggested by Cox and Herrmann (1998) to match the initial slope of the bond stress-versus-slip curves from different experiments. The elastic normal stiffness is a penalty parameter assumed to be $D_{nn} = 2E_c/d_b$. This value is large enough to ensure that the elastic normal deformation is negligible as compared to the plastic normal deformation. The Young's modulus of concrete can be calculated as $E_c = 4{,}730\sqrt{f'_c}$ in MPa (ACI 2011). Regarding the tolerances used to solve the plasticity equations, the iterations are stopped and the solution is accepted when F_A, F_{B^+}, and F_{B^-} are smaller than $1 \cdot 10^{-4}$. Finally, θ in the generalized trapezoidal rule is taken to be 0.5, which has been shown by Ortiz and Popov (1985) to provide good accuracy.

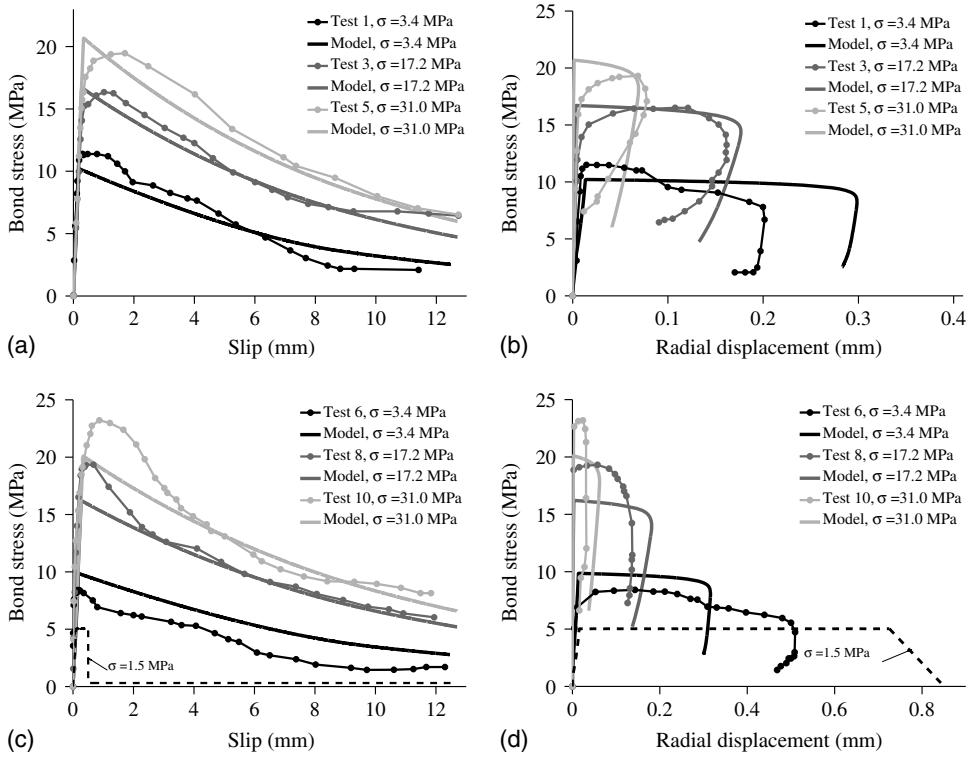

Fig. 6. Comparison of model predictions and experimental results for Malvar's tests: (a) bond stress versus slip in Tests 1, 3, and 5; (b) bond stress versus radial displacement in Tests 1, 3, and 5; (c) bond stress versus slip in Tests 6, 8, and 10; (d) bond stress versus radial displacement in Tests 6, 8, and 10

The interface model successfully reproduces the bond resistance and dilatation obtained by Malvar (1992) for different levels of confinement. The bond stress-versus-slip curves and the bond stress-versus-radial displacement curves obtained in the tests and with the bond-slip model for confining stresses of 3.45 MPa, 17.24 MPa, and 31.03 MPa are compared in Fig. 6. In all cases, plastic displacements are first activated in Mode B (sliding), but as the Mode-B yield surfaces rotate in the $\sigma - \tau$ plane, and the normal confining stress increases, the yield surface corresponding to Mode A (crushing and shearing) is activated and the plastic displacement mode changes. As the plastic slip displacement in Mode A increases, the yield surface shrinks and the bond resistance is reduced, resulting in pullout failure. An additional case with a low confining pressure of $\sigma = 1.5$ MPa has been analyzed to illustrate the capability of the model to simulate bond failure caused by sliding and tensile splitting. In this case, Mode A is never activated and the plastic displacement is solely attributable to sliding on the concrete-steel surface. As shown in Fig. 6, the bond strength is lower and the behavior is more brittle, which is typical of a failure caused by concrete splitting. The bond resistance practically disappears when the slip exceeds the horizontal length of the inclined plane of the rib, l_1, i.e., when the contact occurs on the horizontal plane on top of the ribs and the wedging action is lost. Also, the dilatation is higher as compared to the cases with failures governed by Mode A.

Validation Analyses

The new model has been implemented in the finite element (FE) program ABAQUS as a material (*UMAT*) subroutine to be used with three-dimensional cohesive interface elements. In the implementation, the relative tangential displacement perpendicular to the axis of the bar is restrained with a penalty stiffness. The penalty coefficient used in the validation analyses is equal to $10K_{tt}$. The initial stiffness of the interface model is used for the iterative solution scheme for the nonlinear analysis.

To validate the ability of the interface model to predict the bond strength and bond-slip behavior of bars under quasi-static loading with different loading scenarios and confinement conditions, six tests reported in three different studies (Lundgren 2000;

Table 3. Bond Strengths from Tests and Analyses

Test specimen	Experiment (MPa)	Analysis (MPa)	Prediction error (%)
Lundgren (2000), monotonic test	20.7	18.8	−9
Lundgren (2000), cyclic test	19.3	18.4	−5
Murcia-Delso et al. (2013), monotonic test with $f'_c = 34.5$ MPa	16.3	16.0	−2
Murcia-Delso et al. (2013), monotonic test with $f'_c = 55$ MPa	24.3	25.9	+7
Murcia-Delso et al. (2013), cyclic test with $f'_c = 34.5$ MPa	15.0	15.5	+3
Metelli and Plizzari (2014), monotonic test with 16-mm bar	22.9	21.7	−6
Metelli and Plizzari (2014), monotonic test with 20-mm bar	20.9	21.6	+3

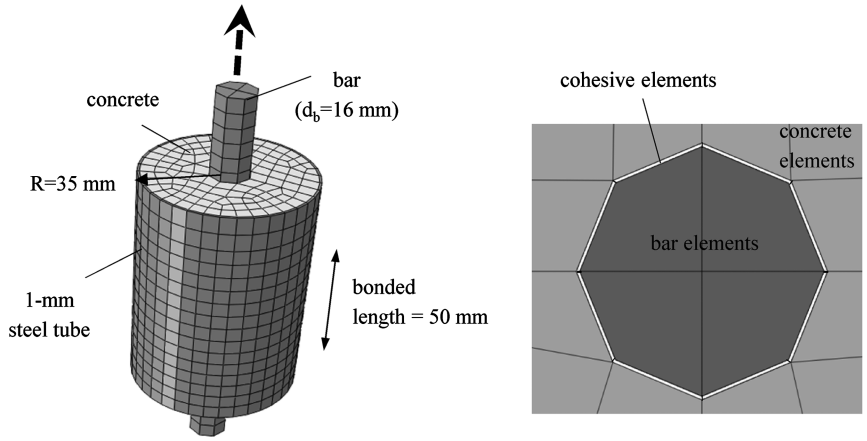

Fig. 7. FE model of Lundgren's test specimens

Murcia-Delso et al. 2013; Metelli and Plizzari 2014) have been replicated with static FE analyses. The test specimens analyzed had the bars bonded over a length between $3d_b$ and $7d_b$ to provide a fairly uniform slip and bond-stress distribution so that the basic bond stress-versus-slip relations could be obtained. The bar and concrete properties in these experiments are shown in Table 1. The bond strengths predicted by the analyses are compared to the experimental results in Table 3. As shown, the model provides good predictions of the bond strengths with a maximum error of 9%.

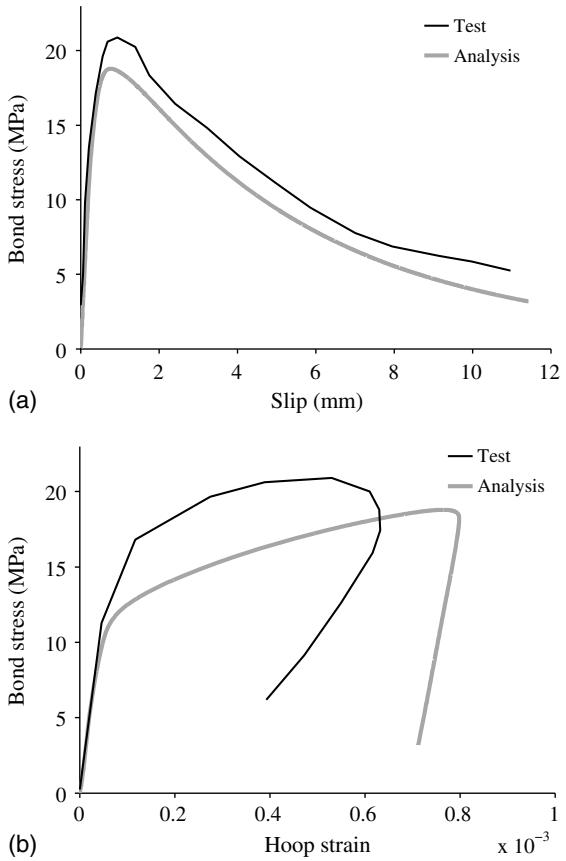

Fig. 8. Comparison of FE analysis and experimental results for Lundgren's monotonic bond-slip test: (a) bond stress versus slip; (b) bond stress versus hoop strain in steel casing

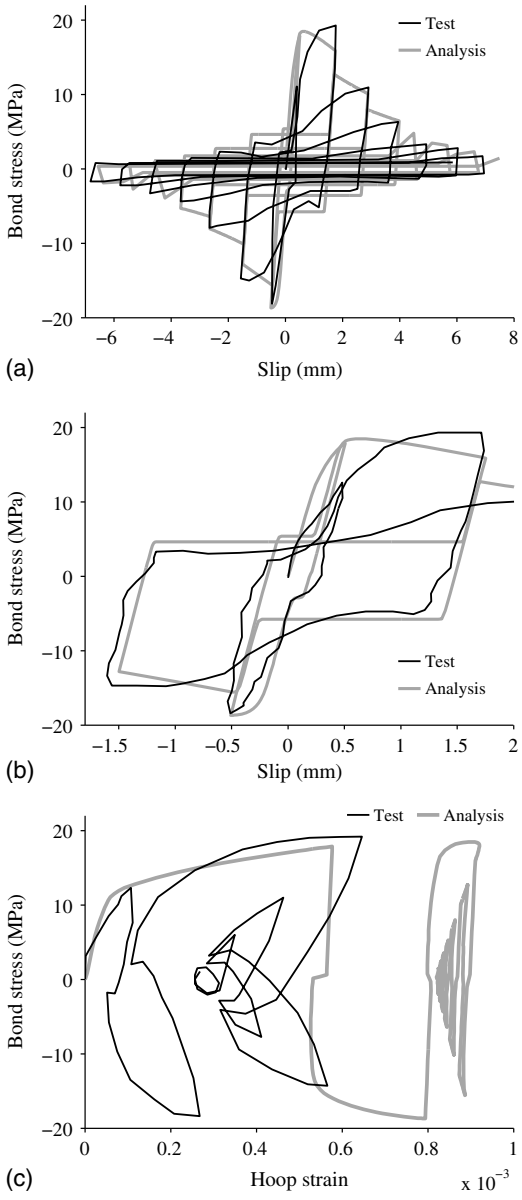

Fig. 9. Comparison of FE analysis and experimental results for Lundgren's cyclic bond-slip test: (a) bond stress versus slip; (b) bond stress versus slip for the first two cycles; (c) bond stress versus hoop strain in steel casing

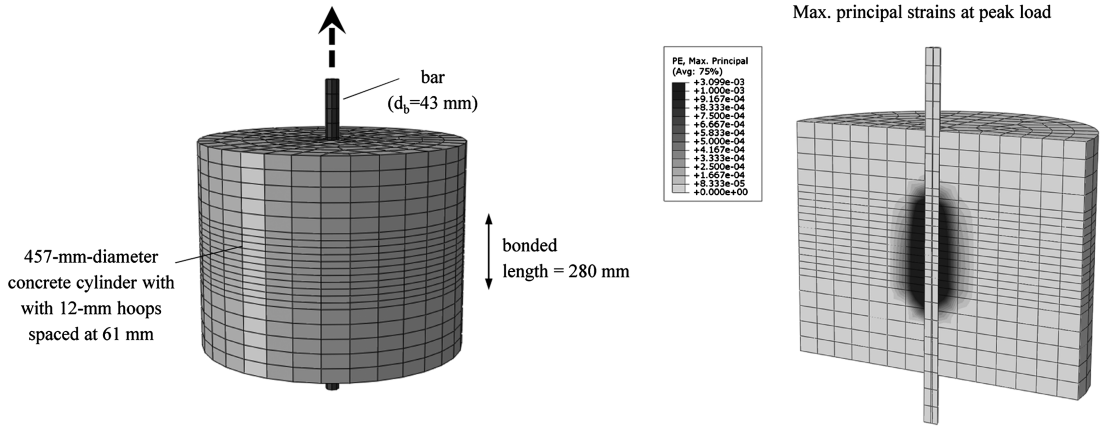

Fig. 10. FE model of test specimens for Murcia-Delso et al.

In the validation analyses, reinforcing bars are modeled with three-dimensional eight-node brick elements (C3D8) and an elastic material with a modulus of elasticity of 200,000 MPa. However, some of the bars yielded in tension in Murcia-Delso et al.'s (2013) tests. For the analysis of these tests, an elastic-plastic material law with nonlinear kinematic hardening available in ABAQUS is used. The steel in these analyses has a yield strength of 493 MPa. The cross section of a bar is idealized as an octagon with an area equal to that of the circular section for the specimen tested by Lundgren (2000), as illustrated in Fig. 7. Concrete is modeled with C3D8 elements and a plastic-damage law available in ABAQUS. This constitutive law is based on the formulations proposed by Lubliner et al. (1989) and Lee and Fenves (1998). The plastic-damage law has been calibrated to the compressive and tensile strengths of concrete as presented in Table 1. The calibration of the other parameters of this law that are independent of the concrete strength is discussed in Murcia-Delso (2013). As shown in Fig. 7, eight-node cohesive crack interface elements (COH3D8) are used to connect the solid elements representing the concrete and the bar, respectively. The parameters for the bond-slip model assume the values presented in Tables 1 and 2. Because of the octagonal cross-sectional shape of the bar model, the surface area of the cohesive elements surrounding the bar is slightly larger than the actual contact surface. To compute the correct magnitude of the bond forces, the stresses at the interface are scaled down by a factor of 0.97 to account for the difference between the perimeter of a circle and that of an octagon of equal area. The same approach has been followed to model the other tests considered in this paper.

The concrete cylinders in the specimens tested by Lundgren (2000) were confined by a steel casing with a wall thickness equal to 1 mm. The casing has been modeled with shell elements and an elastic material with a modulus of elasticity of 200,000 MPa.

The FE analysis and experimental results for a test with monotonically increasing slip conducted by Lundgren (2000) are compared in Fig. 8. The FE model predicts the bond strength and the bond stress-slip relations reasonably well, including the slip at which the peak strength is reached and the rate of the decay of the bond resistance. The hoop strains in the steel casing are fairly well

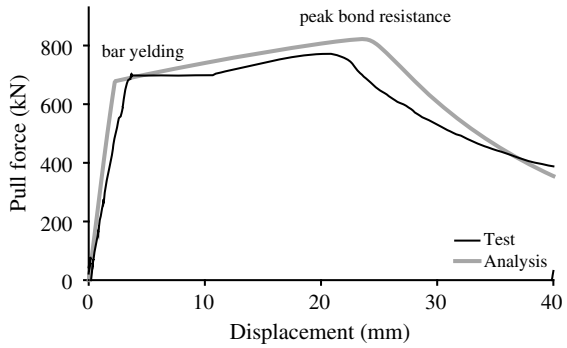

Fig. 12. Comparison of FE analysis and experimental results for Murcia-Delso et al.'s monotonic bond-slip tests with 55-MPa concrete

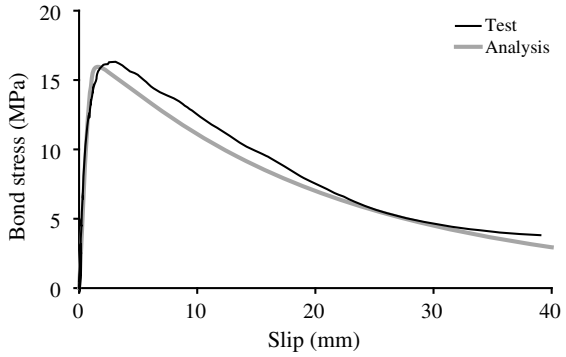

Fig. 11. Comparison of FE analysis and experimental results for Murcia-Delso et al.'s monotonic bond-slip test with 34.5-MPa concrete

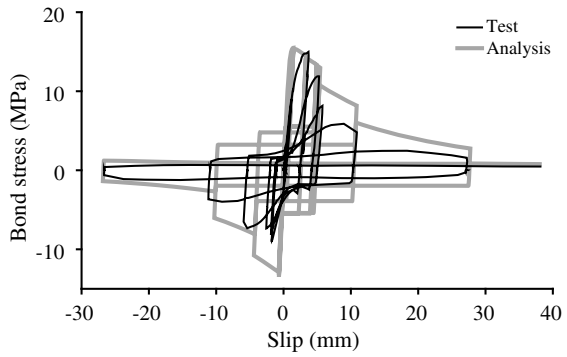

Fig. 13. Comparison of FE analysis and experimental results for Murcia-Delso et al.'s cyclic bond-slip test with 34.5-MPa concrete

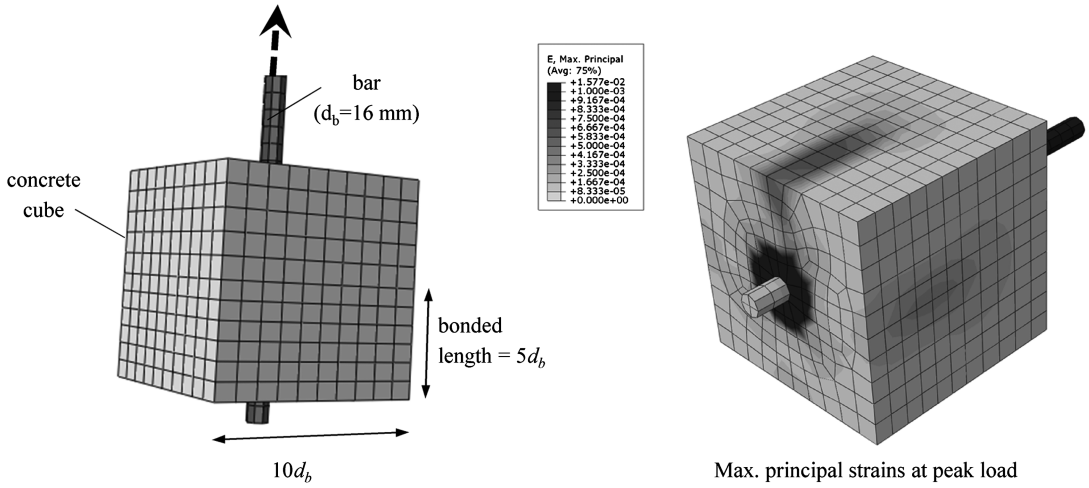

Fig. 14. FE model of Metelli and Plizzari's tests on a 16-mm bar

captured by the model, but their peak value has been slightly overestimated, as shown in Fig. 8. The FE model is also capable of replicating the cyclic bond stress-versus-slip relations in another test, including the decay in the bond resistance (governed by Mode A), and the stresses developed when the slip direction is reversed (governed by Mode B), as shown in Fig. 9. However, when the yield surface for Mode A is re-engaged, the reloading stiffness becomes much higher than that shown in the test because the elastoplastic bond-slip model does not provide a gradual hardening-softening behavior for Mode A. Fig. 9 also indicates that the hoop strain in the steel casing at the end of the cyclic test has been significantly overestimated and the variation of hoop strain during the unloading and reloading is not well predicted. This can be partly attributed to the underprediction of the reversal of shear dilatation by the bond-slip model, and partly to the inability of the concrete model to close the radial splitting cracks that have formed in the concrete cylinder. The latter is related to a limitation of the constitutive law of concrete as discussed in Murcia-Delso (2013).

Three bond-slip tests conducted by Murcia-Delso et al. (2013) on 43-mm bars embedded in well-confined concrete cylinders have been analyzed. The FE model of a monotonic test specimen with $f_c' = 34.5$ MPa is shown in Fig. 10. The maximum principal strains shown in Fig. 10 along a diametric cut of this specimen indicate that bar slip has split the concrete surrounding the bar, but the splitting cracks do not propagate radially. As reported in Murcia-Delso et al. (2013), no splitting cracks were observed in the surface of any of the test specimens. As shown in Fig. 11, the FE analysis and experimental results for the monotonic test specimen with $f_c' = 34.5$ are very similar. The model is also capable of predicting the increase of the bond strength when a concrete with a compressive strength of 55 MPa is used, as shown in Table 3. In the test with the 55-MPa concrete, the bar yielded in tension, and the bond stress-slip relations could not be calculated because plastic strains penetrated inside the bonded length, resulting in a nonuniform slip and bond stress distribution. For this reason, the FE analysis and experimental bond-slip results are compared in Fig. 12 in terms of the pull force-versus-displacement curves for the loaded end of the bar. As shown, the peak bond strength is reached after the bar has yielded in tension. The FE model is also able to capture the bond stress-versus-slip hysteresis curves obtained from a cyclic test with a reasonable accuracy, except for the slope of the reloading branches, as shown in Fig. 13.

To illustrate the capability of the interface model to simulate concrete splitting failures, bond-slip tests carried out by Metelli and Plizzari (2014) have been analyzed. They tested bars of different sizes and rib patterns embedded in concrete cubes with a clear cover equal to $4.5d_b$ and no transverse reinforcement. Two series of tests with 16-mm diameter bars and 20-mm diameter bars, respectively, have been modeled. In each test series, eight identical specimens were tested under monotonically increasing load. The FE model of a test specimen with a 16-mm bar is shown in Fig. 14. All the specimens in these series incurred brittle failures attributable to the splitting of the concrete. The bond strength and splitting

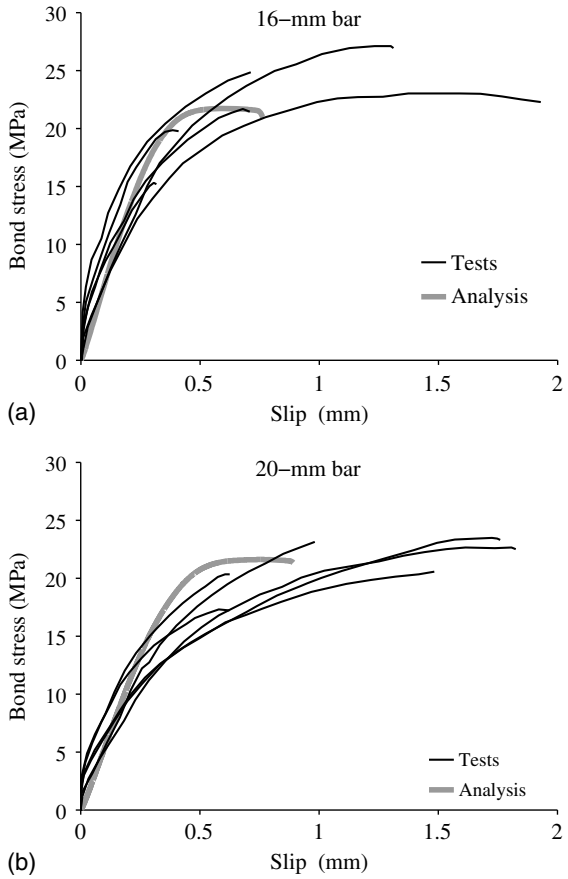

Fig. 15. Comparison of FE analysis and experimental results for Metelli and Plizzari's tests: (a) 16-mm bar; (b) 20-mm bar

failures observed in the tests are well predicted by the FE model. Fig. 14 shows the maximum principal strains obtained in the analysis for a specimen with a 16-mm bar indicating the formation of a splitting crack spreading over the entire concrete cover. The bond stress-versus-slip relations obtained in the analyses are in good agreement with the experimental results, as shown in Fig. 15. However, the analyses are not able to attain very large slip levels because of numerical convergence problems caused by the opening of the splitting cracks.

Conclusions

A new interface model has been developed to simulate the cyclic bond-slip behavior of reinforcing bars in concrete. The model adopts a multi-surface plasticity formulation with nonassociated flow rules. It accounts for two major bond resistance mechanisms. They are the interlocking mechanism that may result in the crushing and shearing of the concrete between the bar ribs, and the frictional resistance mechanism with sliding between the concrete and bar surfaces. Each mechanism is governed by a separate yield surface and flow rule. Nonassociated flow rules are used to simulate the dilatation of the interface induced by the crushed concrete and the wedging action of the bar ribs. A stress update algorithm tailored to handle the multiple yield surfaces of the model has been proposed to solve the nonlinear constitutive equations.

The model has only a few parameters to calibrate. They are determined with the properties of the concrete and the geometry of the reinforcing bar. The capability of the model to accurately predict the bond strengths and the cyclic bond-slip behavior of bars under a wide range of confinement situations has been demonstrated with validation examples. The model can capture bond failures characterized by bar pullout and the splitting of concrete. It can be used in numerical studies to examine the effects of the concrete strength, concrete cover, bar spacing, and transverse reinforcement on the bond behavior of reinforcing bars.

Acknowledgments

The authors wish to thank Fundacio La Caixa and Fundacion Caja Madrid for providing graduate fellowships to the first author for his doctoral studies at the University of California at San Diego, during which the research presented in this paper was conducted. However, opinions expressed in this paper are those of the authors and do not necessarily reflect those of the sponsors.

References

ABAQUS version 6.10 [Computer software]. Providence, RI, Dassault Systèmes.

ACI (American Concrete Institute). (2003). "Bond and development of straight reinforcing bars in tension." *ACI-408R-03*, Farmington Hills, MI.

ACI (American Concrete Institute). (2011). "Building code requirements for structural concrete (ACI 318-11) and commentary." Farmington Hills, MI.

Caballero, A., Willam, K. J., and Carol, I. (2008). "Consistent tangent formulation for 3D interface modeling of cracking/fracture in quasi-brittle materials." *Comput. Methods Appl. Mech. Eng.*, 197(33–40), 2804–2822.

Carol, I., Prat, P. C., and Lopez, C. M. (1997). "Normal/shear cracking model: application to discrete crack analysis." *J. Eng. Mech.*, 10.1061/(ASCE)0733-9399(1997)123:8(765), 765–773.

Cox, J. V., and Herrmann, L. R. (1998). "Development of a plasticity bond model for steel reinforcement." *Mech. Cohesive-Frict. Mater.*, 3(2), 155–180.

Cox, J. V., and Herrmann, L. R. (1999). "Validation of a plasticity bond model for steel reinforcement." *Mech. Cohesive-Frict. Mater.*, 4(4), 361–389.

FIB (Fédération Internationale du Béton). (2000). "fib bulletin 10: Bond of reinforcement in concrete." *Task Group Bond Model*, Lausanne, Switzerland.

Herrmann, L. R., and Cox, J. V. (1994). "Development of a plasticity bond model for reinforced concrete." *CR 94-001*, Naval Facilities Engineering Service Center, Port Hueneme, CA.

Koutromanos, I., and Shing, P. B. (2012). "Cohesive crack model to simulate cyclic response of concrete and masonry structures." *ACI Struct. J.*, 109(3), 349–358.

Lee, J., and Fenves, G. L. (1998). "Plastic-damage model for cyclic loading of concrete structures." *J. Eng. Mech.*, 10.1061/(ASCE)0733-9399(1998)124:8(892), 892–900.

Lotfi, H. R., and Shing, P. B. (1994). "Interface model applied to fracture of masonry structures." *J. Struct. Eng.*, 10.1061/(ASCE)0733-9445(1994)120:1(63), 63–80.

Lubliner, J., Oliver, J., Oller, S., and Oñate, E. (1989). "A plastic-damage model for concrete." *Int. J. Solids Struct.*, 25(3), 299–326.

Lundgren, K. (2000). "Pull-out tests of steel-encased specimens subjected to reversed cyclic loading." *Mater. Struct.*, 33(7), 450–456.

Lundgren, K., and Gylltoft, K. (2000). "A model for the bond between concrete and reinforcement." *Mag. Concr. Res.*, 52(1), 53–63.

Lundgren, K., and Magnusson, J. (2001). "Three-dimensional modeling of anchorage zones in reinforced concrete." *J. Eng. Mech.*, 10.1061/(ASCE)0733-9399(2001)127:7(693), 693–699.

Malvar, J. (1992). "Bond of reinforcement under controlled confinement." *ACI Mater. J.*, 89(6), 593–601.

Metelli, G., and Plizzari, G. A. (2014). "Influence of the relative rib area on bond behavior." *Mag. Concr. Res.*, 66(6), 277–294.

Murcia-Delso, J. (2013). "Bond-slip behavior and development of bridge column longitudinal reinforcing bars in enlarged pile shafts." Ph.D. dissertation, Dept. of Structural Engineering, Univ. of California, San Diego, CA.

Murcia-Delso, J., Stavridis, A., and Shing, P. B. (2013). "Bond strength and cyclic bond deterioration of large-diameter bars." *ACI Struct. J.*, 110(4), 659–669.

Ortiz, M., and Popov, E. P. (1985). "Accuracy and stability of integration algorithms for elastoplastic constitutive relations." *Int. J. Numer. Methods Eng.*, 21(9), 1561–1576.

Puntel, E., Bolzon, G., and Saouma, V. E. (2006). "Fracture mechanics based model for joints under cyclic loading." *J. Eng. Mech.*, 10.1061/(ASCE)0733-9399(2006)132:11(1151), 1151–1159.

Serpieri, R., and Alfano, G. (2011). "Bond-slip analysis via a thermodynamically consistent interface model combining interlocking, damage and friction." *Int. J. Numer. Methods Eng.*, 85(2), 164–186.